ACS OMEGA

Open Access

This article is licensed under CC-BY-NC-ND 4.0

http://pubs.acs.org/journal/acsodf

Review

Advancement in Fabrication and Characterization Techniques of Nanocomposites

Shikha Awasthi,* Suranjan De,* and Sarvesh Kumar Pandey*

Cite This: *ACS Omega* 2024, 9, 19756−19769

Read Online

ACCESS | Metrics & More | Article Recommendations

ABSTRACT: Advancements in the field of materials research have unveiled numerous unparalleled features, such as mechanical properties, clinical advances, interfacial strengthening, and porosities, providing a wide range of applications. The employment of any material begins with fabrication and characterization, demanding expertise for the effective execution of the investigation. This review encompasses the details of the working principles of some significant and frequently used fabrication and characterization techniques for various material categories, including pellets and coatings. The discussion begins with techniques for fabricating materials for various applications. A brief overview of coating synthesis methods can provide intriguing information for researchers in the field of coating fabrication. The report highlights the portrayal of morphological and physiochemical analysis techniques, followed by the estimation of the elastic modulus using nanoindentation and dynamic modulus mapping testing for the materials. Additionally, the review covers theoretical models for observing the elastic moduli of the materials. The review depicts tribological investigations of the materials, aiming to provide insight into fretting wear, pin-on-disc, and microscratch testing. The fundamentals of electrochemical characterization are presented, including the appraisal of linear polarization and potentiodynamic polarization as well as electrochemical impedance spectroscopy. Furthermore, the magnetic behavior was examined by using a vibrating sample magnetometer (VSM), and the estimation of magnetic domains in the materials was conducted through magnetic force microscopy. Thus, the report suggests that readers, especially beginners, can gain a comprehensive understanding of the extensive prospects associated with the fundamental principles of material synthesis and characterization.

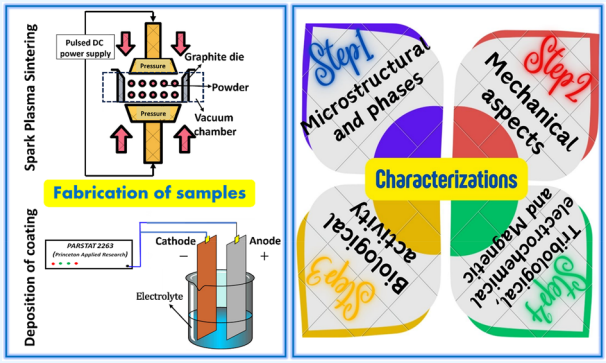

1. INTRODUCTION

Nanocomposites deliver potential on entirely new scales for tackling difficulties encompassing the pharmaceutical, packaged food, electronic device, and energy industries.[1,2] A nanocomposite is a solid substance made up of several phases, at least one of which has dimensions in the nanoscale range, in one, two, or three dimensions.[3,4] The constructive integration of diverse elements is accomplished by nanoscale phase transformation. Nanocomposites contain nanomaterials such as nanoparticles, nanofibers, and nanoclays.[5] Notably, the characteristics of the material change when the size of the parts goes below a specified threshold, also known as the "critical size".[5,6] Reducing the material size to the nanoscale improves characteristics via critical phase interface interactions. Nanocomposites are the next generation of composites due to their high surface/volume ratio, paving the way for smaller filler sizes and distances between fillers. The surface-area-to-volume ratio in nanocomposite preparation affects the structure−property connection. Nanocomposites, which contain at least one nanometric component, preserve basic traits while overcoming flaws and introducing unique properties.[7,8] These materials are a multiphase crossover of reinforcing (dispersed phase) and matrix (continuous phase) materials, including fibrous and metallic/polymeric components.[9−12] Additionally, nanocomposites have enhanced mechanical characteristics, such as high ductility and resilience to scratches, as well as improved spectral characteristics based on particle size.[13,14] On the other hand, the disadvantages of using nanocomposites are mostly due to issues with hardness and impact endurance caused by the integration of nanoparticles into the bulk matrix of the composite. These problems include a lack of understanding of the formulation, properties, dispersion, and characterization techniques to attain accessibility.[15−17] The purpose is to outline which raw material and technology are most suitable for the fabrication and

Received: December 14, 2023
Revised: March 27, 2024
Accepted: March 28, 2024
Published: April 23, 2024

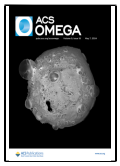

© 2024 The Authors. Published by American Chemical Society

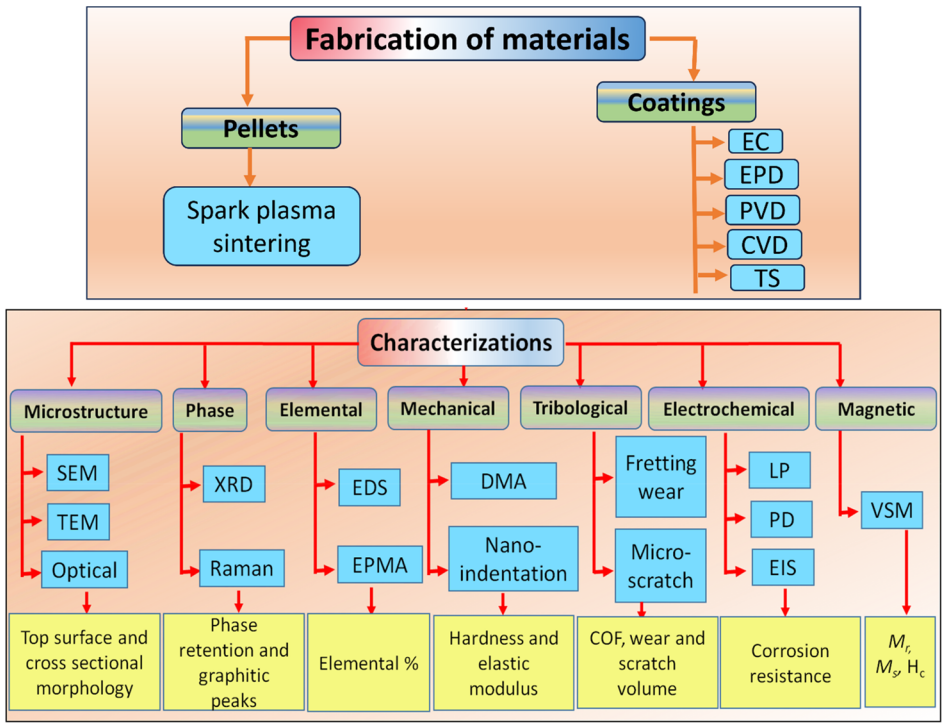

Figure 1. Schematic representation of the substantial advanced techniques for the fabrication and characterization of materials. Original illustration. Abbreviations: EC, electrochemical deposition; EPD, electrophoretic deposition; PVD, physical vapor deposition; CVD, chemical vapor deposition; TS, thermal spray; LP, linear polarization; PD, potentiodynamic polarization; EIS, electrochemical impedance spectroscopy; VSM, vibrating sample magnetometer.

characterization of certain nanocomposites. The engineering operations and implementations encompass a huge variability of materials that need to be characterized to recognize their physical, mechanical, chemical, magnetic, tribological, and biological properties. The multiscale approach is functionalized on the design of the materials. The advancement in materials synthesis and characterization severely relies on their capacity to attain functional and structural information on constituents across multilength scales and dimensions. The review of the principle of fabrication and characterization techniques is essential for beginners and advanced scientists/engineers to offer a better understanding of the technique for a particular application.[18,19] Fundamentally, materials are the index of social development. The stone age, bronze age, and iron age of mankind's evolution have indeed been allied to metal and materials. A global perception is obligatory for the materials based on the indication of existing development.[20] The traditional use of metal and alloys turned into structural and functional materials, ceramics, and manmade composites. The materials of different categories are mandatory in our endeavor to accomplish improved human life. Effective materials mandate adequate knowledge of the synthesis and characterization of materials. The meaningful visualization of materials can help in correlating the performance behavior of materials to the characterization and fabrication parameters of materials. Various characterization techniques are utilized through different possible approaches. The surface morphology of the materials is accessed by scanning electron microscopy (SEM), transmission electron microscopy (TEM), atomic force microscopy, etc. The top surface characterizations are followed by investigations related to phase (X-ray diffraction) and functional groups (Fourier transform infrared spectroscopy) of the materials. The application-based characterizations lead to mechanical, tribological, magnetic, electrochemical, and biological observations. The expertise and contribution of material scientists, chemists, physicists, and instrumentation specialists enable all these techniques to be successful for materials characterization. The assortment of appropriate techniques for specific materials and applications is decisive for the efficacious execution of the research, which can be retrieved through a report covering noteworthy production and characterization approaches. The reports related to the discussions on the working principles of fabrication and characterization techniques are lacunae in the literature. To the best of our knowledge, it is only state-of-the-art in the principles of synthesis and characterization techniques where an extensive effort has been made to explore the most important methods along with the discussion on theoretical aspects of morphological and mechanical features of the materials. Briefly, it can be inferred that this review aims to be a comprehensive, authoritative, critical, and accessible review of general interest to the chemistry community because this comprehensive review article will be very significant for the chemists, materials scientists, physicists, industries, and innovators who are working in any field of material engineering/science as well as for awareness of the global audience (beginners as well as nonspecialists). Figure 1 gives the essence of some imperative advanced techniques for the fabrication and characterization of the materials. An outlook of the schematic presents two types of material synthesis, in the form of either pellets or coatings. Pellets can be manufactured generally by using a spark plasma sintering process, while various methods are utilized for the synthesis of the coatings such as electrochemical deposition, electrophoretic deposition, physical vapor deposition, chemical vapor deposition, and deposition of coatings using a thermal spray technique. Moreover, the schematic focuses attention on the various characterization

https://doi.org/10.1021/acsomega.3c09981
ACS Omega 2024, 9, 19756−19769

techniques, including microstructure, phase, elemental, mechanical, tribological, electrochemical, and magnetic characterizations. The interpretation of the working principles on the aforementioned practices is stated in the consecutive sections.

2. SYNTHESIS OF MATERIALS

2.1. Spark Plasma Sintering for the Production of Pellets. Sintering is a process for making things out of powders, which requires heating materials in a furnace below their melting temperature, allowing atom diffusion to form bonds. As a result, independent particles of the powder are consolidated into a dense, compact structure. While sintering is a popular option for ceramics, there are other techniques available, including Spark Plasma Sintering (SPS), Conventional Sintering (CS), and Microwave Sintering (MS). SPS is a unique method that drastically reduces the sintering process, taking just minutes to do what conventional sintering may take hours or even days to complete. This fast sintering is facilitated by SPS's capacity to quickly achieve extremely high heating rates, which is aided by internal heating of the sample rather than external heating employed in traditional sintering techniques. Furthermore, because of the short holding period at the sintering temperature, which typically lasts only 5−10 min, SPS has substantially shorter sintering timeframes, in contrast to the potentially extensive durations of classical sintering, which can last several hours. The normal rate of heating in traditional furnaces is 5−8 °C/min, with a maximum temperature of 10 °C/min. Normally it takes 2−4 h or longer to attain a temperature of 1200 °C. SPS, on the other hand, may easily reach heating speeds of more than 300 °C/min, allowing for the achievement of an ideal temperature of 1200 °C in as little as just 4 min. The simultaneous application of temperature and pressure induces a substantial rise in densification, giving a dense compact at sintering temperatures that are 200−250 °C lower than those generally used in traditional sintering processes. The suppression of coarsening and grain expansion in the context of SPS permits the quick accomplishment of high relative densities in a much-reduced duration. This property is highly beneficial for sintering nanosized powders since it reduces significant grain formation, which is a major issue in traditional sintering techniques. As a result, SPS is a productive method for producing nanostructured ceramics or nanocomposites with improved densification and fewer structural flaws. These nanostructured composite materials, in turn, have extraordinary mechanical qualities, including increased strength and hardness. SPS is also a laboratory-based manufacturing process that is extensively employed in biomaterial synthesis.[5] The basic technique for traditional sintering requires first externally creating a green compact with a proper die and hydraulic equipment to deliver the requisite pressure. This green composite is then exposed to the sintering process within a furnace. The SPS technology, on the other hand, provides a more simplified methodology. The powder is put directly into graphite dies, which are subsequently encased with appropriate punches. The complete system is inserted directly into the SPS chamber with spacers optional if necessary. The chamber is sealed, and the desired sintering environment (such as vacuum or argon) is set up within it. Configuring the control unit with the proper software starts the process of sintering. As opposed to traditional furnaces, one significant advantage of SPS is the simplicity of environment control. With amazing efficiency, this approach accommodates a wide range of materials, even those that are difficult to densify. In comparison to traditional sintering, SPS efficiently reduces undesired sintering reactions due to its quick heating rates and minimum holding durations. As a result, this method aids in the prevention of the creation of undesired product stages.[21]

2.2. Fabrication of Coatings. Coatings are crucial components in protecting the surface of the material from wear and electrochemical corrosion in the majority of metal applications. Different manufacturing techniques include electrochemical processes, chemical vapor deposition (CVD), physical vapor deposition (PVD), and thermal spraying (TS) (Figure 1).[22−24] The most economical procedures include electrochemical (EC) and electrophoretic deposition (EPD), which have control deposits with a thickness of 240 m in 1 h and cost-effective control deposits between 25 and 100 nm.[25] Along with the managed film qualities, coatings can be deposited at room temperature. Therefore, these deposition techniques that use the dispersion of hard particles in the metallic matrix have fully grown in recent years for use in chemical, mechanical, and electrical applications.[26,27] The review deals with the deliberation of the working mechanism of EC, EPD, PVD, CVD, and TS technologies.

2.2.1. Electrochemical (EC) and Electrophoretic Deposition (EPD) of Coatings. A conducting electrode is submerged in an electrolyte during the electrochemical deposition process. Electrolysis, commonly termed a bath, is a chemical transformation that occurs in an electrolyte when an electric field is applied (Figure 2). The bath (such as Watts or sulfamate baths)

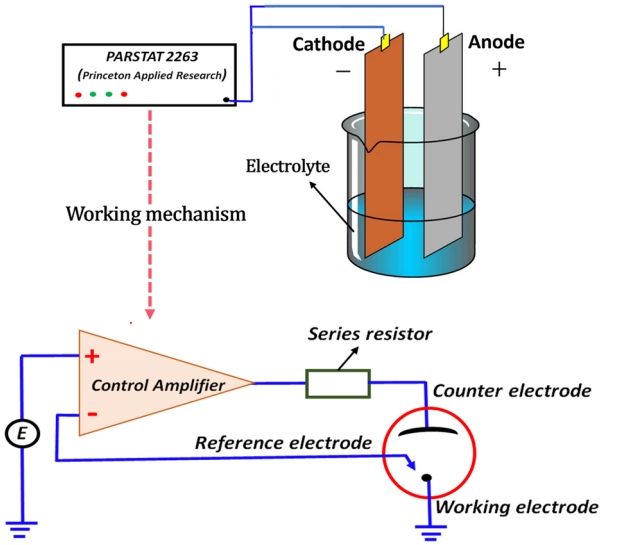

Figure 2. Schematic presentation of the experimental setup with the working mechanism of the potentiostat for electrochemical and electrophoretic deposition of coatings. The concept was adapted from ref 35 and redrawn by the authors.

contains inorganic salts or the salts of complex compounds in an aqueous medium.[28] Direct current electrochemical deposition, pulse reverse current electrochemical deposition, and pulsed electrochemical deposition are some of the methods for electrochemical deposition. Pulsed electrochemical deposition is one of the most widely used techniques in this context because of its adaptability when using pulse parameters which reduces process limitations (has adaptability when varying process parameters), and the higher deposition rate enhances the physical features and mechanical performance of the coatings.[29]

https://doi.org/10.1021/acsomega.3c09981
ACS Omega 2024, 9, 19756−19769

The working mechanisms of EC and EPD comprise an electrolytic cell and electrodes, which are connected to a potentiostat. For instance, Ni salts such as $NiSO_4{\cdot}7H_2O$ and $NiCl_2{\cdot}6H_2O$ are utilized in the electrolytic bath to prepare the Ni coating on the Cu substrate. Copper assists as the cathode or working electrode, and nickel works as the anode or counter electrode (Figure 2). Before the deposition process, the copper cathode is mechanically polished, and the residual region can be marked with Teflon tape to reveal a target area of 1 cm^2. Saccharin addition in an electrolytic solution is utilized to improve the mechanical characteristics and refine the microstructure.[30,31] The surface morphology of Ni coatings is improved by the addition of compounds such as sodium dodecyl sulfate (SDS) and boric acid. During electrophoretic deposition, boric acid absorbs on the cathode and forms nickel borate, which raises the excess potential of hydrogen and reduces the evolution of H_2 while also increasing the deposition potential of Ni^{2+}. Additionally, the SDS improves nickel reduction on the cathode with the least amount of surface pitting.[32,33] The current density, pulse current frequency ($(t_{on} + t_{off})^{-1}$), duty cycle ($t_{on}/(t_{on} + t_{off})$), on-time ($t_{on}$), and off-time ($t_{off}$) of the current are used to control the pulsed current waveform. The parameters for electrophoretic deposition, including temperature, pH level, current density, and salt content in the electrolytic solution, are optimized prior to the deposition of the coatings of desired materials.[34]

The principle of the potentiostat involves measurements of the potential difference between the reference and working electrodes by applying the current through the counter electrode (Figure 2). However, the control amplifier adjusts the voltage of the input source (E) and output source to preserve the equilibrium throughout the process by maintaining the voltage between the working and reference electrodes (Figure 2).

2.2.2. Physical Vapor Deposition (PVD) of Coatings. PVD technology is well-known for imparting corrosion and wear resistance to material surfaces by depositing thin protective layers that are exposed to harsh environments. It has a wide range of uses, from aesthetic objects to industrial components.[9] One of the most notable benefits of this approach is the ability to customize the mechanical, corrosion, and cosmetic properties of the coating layers as desired. PVD takes place in a high-vacuum environment when solid or liquid materials move into a vapor phase, accompanied by metal vapor deposition. This deposition method produces thick and solid films. Sputtering and evaporation are two of the most well-known PVD methods. Because PVD coatings are naturally thin, there is a continual need for multilayered coatings, with a careful choice of materials. Beyond their ornamental uses, many components with PVD coatings are subject to severe levels of wear and abrasion, which can impair the coating layer's integrity. As a result, the corrosion resistance of the components is reduced, making them more sensitive to corrosive substances.[36] Coating development is predominantly driven by a physical evaporation process in this approach. Evaporation requires thermal energy, which may be delivered by a variety of sources including electron beams, laser beams, molecular beams, heating wires, and others. The atoms of the source material—solid or liquid—are raised to their corresponding evaporation points by this thermal energy. The vaporized atoms are then transported by the vacuum and deposited on the substrate.[36]

2.2.3. Chemical Vapor Deposition (CVD) of Coatings. A different kind of vapor deposition is chemical vapor deposition (CVD). This approach is frequently employed in the semiconductor industry for creating robust, high-quality, and highly resistant coating layers on a variety of substrates.[7] CVD is especially well-suited for mechanical components that are in constant contact and must be protected against corrosion and wear. The substrate of interest also recognized as a "wafer", receives exposure to many volatile material precursors throughout the process of CVD, which triggers a chemical reaction that leads to the deposition of a layer on the surface of the material. It is crucial to keep in mind that while certain byproducts of these chemical reactions could still be present within the chamber, they are continually being expelled by the airflow from a vacuum pump. In the CVD setup, vaporized CVD ingredients are provided from the right side and heaters maintain the substrate and vaporized materials at a high enough temperature to enable chemical interaction.[36] There are various CVD approaches based on substrate heating, material properties, and the type of plasma employed for vaporizing the components. There are arguments both for and against CVD over PVD based on the application. The substrate in the CVD process is heated to 900 °C, avoiding the use of temperature-sensitive materials. PVD provides a solution for these types of materials. However, because just the heated zone may be coated with CVD, there is a minimum material waste.[36]

2.2.4. Thermal Spray Technique. The TSC is a collection of techniques that liquefy carefully chosen materials using various heat sources, such as plasma, electricity, or chemical combustion, and then project the semisolid or molten material onto a surface to create a protective film. The dependability of these coatings in providing corrosion and wear resistance has been well established. In this method, the materials are heated to a semisolid or molten state and then propelled onto the substrate at a high velocity using chemical combustion or plasma discharge methods. In comparison to electroplating, PVD, and CVD technologies, thermal spray coating processes have a far wider range of possible thicknesses, from 20 m to several millimeters.[37] Besides, a variety of materials, including refractory metals, metallic alloys, composite ceramics, and polymers, may be employed as feedstock for thermal spray coatings. All of these materials have the ability to efficiently cover a substrate's relatively high surface area. Considering their characteristics and processing requirements, thermal spray coatings are divided into a number of kinds. The most typical are high-velocity air fuel (HVOF), wire arc spraying, plasma, detonation, warm/cold, flame, and high-velocity oxyfuel (HVAF).[36]

3. MICROSTRUCTURAL CHARACTERIZATIONS AND VORONOI TESSELLATION

Optical microscopy can be used to examine the homogeneity and thickness of materials (such as pellets or coatings), while scanning electron microscopy (SEM) and transmission electron microscopy (TEM) are used to examine the surface morphology of the materials.

3.1. Scanning Electron Microscopy for the Characterization of Surface Morphology of the Materials. SEM is a flexible tool for imaging solid objects and determining their elemental makeup. SEMs generally have a low-end magnification range of 20−50×, with the greatest magnification being limited mostly by the size of the electron beam, which can be one million (10^6) times larger. These magnification levels allow for the measurement of elements ranging in size from millimeters to nanometers. The sensitivity of high-end scanning electron microscopes is around 0.5 nm. The primary SEM data are the secondary electron image (SE image), showing topography by

https://doi.org/10.1021/acsomega.3c09981
ACS Omega 2024, 9, 19756−19769

mapping secondary electron emissions based on spatial positions. The number of emitted secondary electrons is influenced by the surface angle, which corresponds to the sample's topography due to the electron beam's perpendicular incidence over the analysis area. Backscattered electrons (BSE) are the second most common type of data collected in SEM imaging, portraying backscattered electron emissions based on spatial positions. The secondary electron image (SE image) is the principal SEM data, and it depicts topography by mapping secondary electron emissions, depending on spatial placements. The surface angle, which corresponds to the sample's topography owing to the electron beam's perpendicular incidence over the examination region, influences the quantity of released secondary electrons. Backscattered electrons (BSE) are the second most often obtained data type in SEM imaging, depicting backscattered electron emissions, depending on spatial locations. It is typically not possible to evaluate sample roughness from a top-down perspective in SEM images when electron emission is related to spatial location, because electron emission may not correspond with height. Even in circumstances when electron emission does rely on height, such as in secondary electron pictures, estimating the height directly from electron emission data is frequently impractical. A cross-sectional view of the sample is typically required to evaluate the roughness. SEM not only records sample morphology but also creates and collects distinctive X-rays by using energy-dispersive X-ray spectrometry (EDS). EDS illuminates the elements inside the sample and generates element distribution diagrams by spatially mapping X-ray data. Typically, EDS can identify components at levels as low as 0.5% by weight inside the X-ray generating volume.[38]

3.2. Transmission Electron Microscopy. Transmission electron microscopy (TEM) is an exceptional technology for exploring a wide range of material properties with extremely high spatial resolution. This includes atomic-level knowledge of the shape, size distribution, crystal structure, strain, defects, and chemical data. The interaction of electrons with the material offers all of the information obtained by TEM. Images are produced by detecting electrons that have passed through a thin object, thus the name "transmission" electron microscopy. TEM materials must be exceedingly thin to allow electron transmission, frequently with a thickness of less than 200 nm, depending on the sample's composition and data necessary to perform TEM characterization.[38] Transmission electron microscopy encompasses a number of techniques, each of which delivers distinctive knowledge to the materials. The following are some examples of these methods.

3.2.1. High-Resolution TEM (HRTEM). This technique is used to deliver atomic-level pictures by exploiting the interference between transmitted and diffracted beams. HRTEM is very handy for seeing atom configurations in the projection.

3.2.2. Energy-Filtered TEM (EFTEM). This technique is used to map the elements and chemicals. By reduction of inelastically dispersed electrons, it may also be utilized to increase contrast in pictures and diffraction arrangements.

3.2.3. Energy-Dispersive X-ray Spectroscopy (EDS). This method is useful for identifying the chemical composition of the surface of a specimen. It facilitates material chemical or compositional characterization.

3.2.4. Selected-Area Electron Diffraction (SAED). This is used to characterize crystal shapes, determine the direction of nanowire development, and create ideal conditions for dark field imaging.

3.2.5. High Angle Annular Dark Field (HAADF) TEM. This approach is effective for locating and describing nanoparticles where heavier atoms provide a higher contrast in the image.

3.2.6. Bright Field (BF) TEM. In bright-field TEM images are used to identify the precise structure of the materials where crystalline structures or high mass density appear as black patches.

3.2.7. Dark Field (DF) TEM. Dark field (DF) pictures are used to identify a pattern of nanocrystal sizes as well as the existence of crystalline abnormalities.

3.2.8. Electron Energy Loss Spectroscopy (EELS). EELS is used to detect atomic composition, estimate chemical bonding, and examine surface features.

3.3. Atomic Force Microscopy (AFM). A scanning probe microscope (SPM) is flexible equipment that can provide exact height pictures of solid sample surfaces while also giving information on their mechanical, electrical, and magnetic characteristics. This device works by placing a tiny physical probe close to the sample and measuring its reactions as it scans laterally over the surface. Scanning probe microscopy is a broad term that encompasses a variety of probe methods such as scanning tunneling microscopy and magnetic force microscopy. Surface imaging is commonly used in atomic force microscopy (AFM) to examine aspects such as shape, roughness, or mechanical properties. The vast majority of commercially available probes are made of silicon (Si). These probes are generally made up of a cantilever beam with an etched silicon sharp tip. The nature of the data gathered is determined by the type of probe used. A typical etched Si cantilever/tip is often used for general-purpose height imaging. When specific data, such as magnetic information, are required, a magnetized tip can be created by covering a normal tip with a magnetic substance.[38]

The tapping mode of operation, which is quite common, involves a vertical cantilever oscillation. During the bottom phase of the oscillation, the tip "taps" the sample by getting near enough to touch it. To preserve a steady magnitude of oscillations and a constant force between the tip and the sample, a feedback loop is used. The most common sort of data produced by Atomic Force Microscopy (AFM) is a height map. It is important to note that the word "height" map can be a little deceptive because it is determined by monitoring how the feedback loop moves the probe to keep the force between the tip and the sample constant. Images produced by an atomic force microscope (AFM) generally have a field of view of less than 10 mm, a maximum scan size of around 100 mm, and the capacity to resolve atomic sizes. Ultrahigh-vacuum (UHV) conditions are often needed for AFM to achieve atomic resolution. AFM pictures are characterized by their field of view rather than their magnification, and the resolution is affected by the physical probe's sharpness and shape. It is simple to determine sample roughness because AFM pictures offer absolute height information. However, the physical features of the tip might affect data accuracy, making protrusions look bigger and wells appear smaller than they are. Sharp sample characteristics can sometimes image the tip itself, which is generally evident and indicates probable tip damage. AFM tips are disposable and will become worn throughout imaging. The tip and cantilever qualities are generally defined by the intended data type and the modulus of the sample.[38]

3.4. Voronoi Tessellation. To reconnoitre the distribution and area of nano/microparticles in the bulk matrix, Voronoi tessellation (VT) can be the best tool for all types of materials. The image-processing technique known as VT creates a cellular-

https://doi.org/10.1021/acsomega.3c09981
ACS Omega 2024, 9, 19756−19769

like structure in which each particle is connected to a specific area called a Voronoi cell.[39] The image investigation comprises the transformation of the SEM images into black-and-white pictures by using appropriate threshold values after changing them to greyscale. The black area in the attained picture shows the nano/microparticles (for example, diamond particles in the Ni matrix) (Figure 3a). The identification of the centroids of all

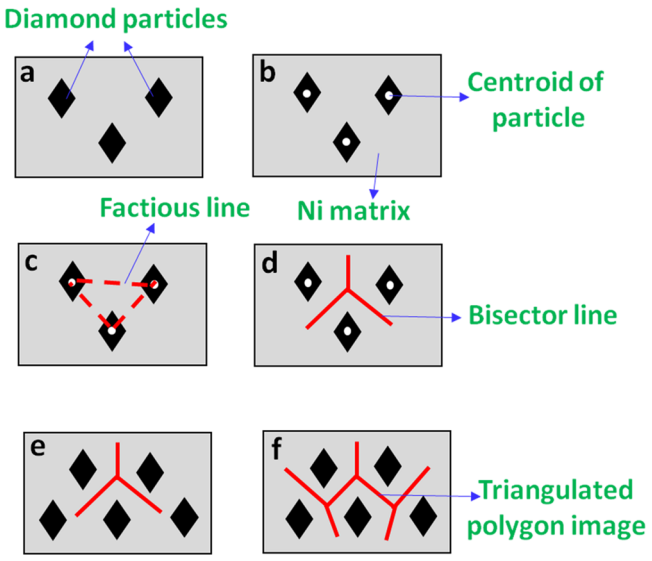

Figure 3. Schematic presentation of the mechanism of Voronoi tessellation. (a) Conversion of the black-and-white image through the appropriate threshold values after converting it to greyscale. The black region in the obtained image represents the nano/microparticles. (b) Identification of centroids. (c) The joining of nearest neighbors by the center of the line (factious line). (d) Drawing of bisector line. (e) Propagation of bisector lines. (f) Creation of polygons around the centroids. Original illustration.

individual particles is done, and Voronoi tessellation of these centroids is used as a standard point (Figure 3b). The center of the line (factious line) linking the nearest neighbors (Figure 3c), and a bisector line further can be drawn with the exclusion of the factious line (Figure 3d), which on following the same trend (Figure 3e) creates the polygons around the centroids (Figure 3f). Nearest neighbors relative to each centroid can be identified using VT, and the Euclidean distance can be calculated amid all pairs of neighboring centroids. The area of the polygon and the fraction of particles can be obtained as the pixel count.

After the processing of the materials, physiochemical characterizations are estimated in order to detect the phase retention and presence of functional groups in the fabricated materials.

4. PHYSIOCHEMICAL CHARACTERIZATIONS OF THE MATERIALS

4.1. X-ray Diffraction (XRD). A very supple method, X-ray diffraction (XRD) yields chemical information for phase analysis as well as elemental analysis. XRD is very noteworthy for texture analysis and stress measurements, in addition to chemical characterization. XRD analysis requires crystalline samples, although it can also determine a polymer's degree of crystallinity. Although XRD has historically been used to analyze bulk samples, new optical techniques have made it possible to use XRD for thin-film examination, as well. The method makes use of the Bragg diffraction law. The XRD technique is also significantly functional for polymeric and ceramic samples.[40,41] The primary method for determining the kind of bonding and the order of crystalline organization in an amorphous polymeric nanocomposite is X-ray diffraction. A polymeric nanocomposite exhibits excellent X-ray diffraction performance due to the formation of crystalline behavior in these materials after creation. XRD can identify changes in the sample's microstructure and interlayer spacing. In the literature, the polymeric samples of graphene oxide and poly(vinyl alcohol) were fabricated and characterized. Additionally, XRD was used to characterize the composites. The distinct peaks of the polymeric matrix vanished, and XRD revealed a single peak when reduced graphene oxide and graphene oxide were added to the polymeric matrix. The outcomes of the study revealed an enhanced crystallinity with the accumulation of reduced graphene oxide and graphene oxide in the bulk polymer.

4.2. Fourier Transform Infrared (FTIR). Infrared (IR) spectroscopy is an effective approach for thorough material examination, providing insights into a chemical's molecular structure, dynamics, and surroundings. FT-IR finds extensive applications because it is simple to use, widely applicable, affordable, time- and money-efficient, safe, nontoxic, internationally accessible, and requires little space. When analyzing industrially created materials, FTIR spectroscopy is an advanced method for inspection of quality, and it tends to be used as the first stage of the material inspection stages. In addition, a crucial method for characterizing polymeric and biopolymeric materials is FTIR spectroscopy. The FTIR technology has been demonstrated to be beneficial in identifying and characterizing homopolymers, copolymers, and polymer composites. It was also effectively utilized to assess the polymerization process and characterize the polymer structure, surface, degradation, and modification. A fluctuation in the characteristic shape of the absorption region implies a modification in the structure of the material or the presence of contaminants. FTIR spectroscopy shows itself as an unusually adaptable instrument for assessing the surface properties of diverse materials among the numerous nondestructive testing procedures.[42] Moreover, it enables real-time monitoring of chemical reactions at the surface of the material, allowing for a thorough analysis of how these processes alter in response to various applications. Additionally, FTIR spectroscopy contributes to the advancement of solid-state physics. In addition to chemical analysis, this method might be used to analyze the infrared absorption produced by electronic carriers. In addition to the conventional Drude model, this absorption, which is sometimes disregarded in vibrational studies, is proportional to the free carrier density and has a direct relationship with the square of the wavelength. A specialized configuration must be connected with the spectrometer in order to adequately leverage its characteristics.[38]

4.3. X-ray Photoelectron Spectroscopy (XPS). XPS, additionally referred to as Electron Spectroscopy for Chemical Analysis (ESCA), is an experimental approach of evaluating the energy of released electrons after blasting a specimen with X-rays. MgK at 1253.6 eV and AlK at 1486.6 eV are two common X-ray sources for XPS. Furthermore, utilizing a UV laser at 21.2 eV, large count rates for the low-energy region may be obtained, delivering critical data on the valence band. Only the electrons near to the surface may be released regardless of suffering energy loss owing to collisions with other atoms since X-rays can penetrate the specimen's surface to a depth of a few micrometers. The connection between the kinetic energy

https://doi.org/10.1021/acsomega.3c09981
ACS Omega 2024, 9, 19756−19769

(KE) and binding energy (BE) of these released electrons is recorded, and the amount of binding energy may be calculated.

Scanning through the kinetic energy range from 0 eV to the incoming X-ray energy delivers an energy spectrum. This spectrum is unique to each element, allowing for the detection of components included in the sample's top 1−2 nm. The detection limit of XPS is roughly 0.1% atomic, making it especially responsive to elements with higher atomic numbers. The energy resolution of the spectrometer successfully identifies distinct chemical bonds such as C−C, C−O, and O−C═O. The percentage of each bond in the material is represented by the area under each peak. Because XPS is primarily used to explore the first few monolayers, sample purity and processing are critical to achieving a good outcome. For storage, glass or fluoro ware containers are preferable over plastic bags. XPS is suited for a wide range of materials, but it has some restrictions: a solid sample and vacuum compatibility are required. Powder may be taped down, and liquids can be evaporated on a silicon substrate.[38]

4.4. Raman Spectroscopy. Following the 1928 finding of the Raman effect, Raman spectroscopy is currently undergoing a renaissance that has led to the development of several cutting-edge methods. Over the past few decades, exciting advancements in optical, quantum mechanical, and spectroscopic areas have opened up new avenues for nanomaterials research. The Raman spectroscopic technique is one of the most effective analytical tools for characterizing the structure of numerous types of materials like carbonaceous allotropes, polymers, ceramics, etc. The characterization of structural features, chirality, diameter, and determination of sp^3 and sp^2 fractions in graphite, graphene, single-walled carbon nanotubes, and diamond-like carbon, respectively, can be effortlessly accessed by using Raman spectroscopy.[43−45] The characterization of polymer materials by the Raman spectroscopic method is important, as it acquires a decent spectrum with minimum handling of the sample. It has several uses in polymer chemistry, polymer materials, and composites. A few of these uses include mapping polymeric phases, predicting physical properties, and monitoring polymerization reactions.[46] The fundamentals of Raman spectroscopy involve the presence of an elastically scattered beam and the weak light reflections with marginally dissimilar frequencies from υ_0 (nonelastically scattered lights) when a substrate is irradiated by a beam of the laser having frequency υ_0 and energy E_0 ($E_0 = h\upsilon_0$, where h is the Planck constant). The frequency shift υ_1 (s^{-1}) corresponds to one of the substance's vibration modes. The Raman shift (cm^{-1}) is equal to υ_1/c, where c is the speed of light. Although there is a frequency difference between the Stokes and anti-Stokes sides of a Raman mode in the materials due to a dispersive effect of the Raman mode, the scattered light with $\upsilon_0 - \upsilon_1$ is called Stokes scattering and that with $\upsilon_0 + \upsilon_1$ is called anti-Stokes scattering. The Stokes scattering is typically used for Raman measurements for the materials.[47,48] The observation of the mechanical, tribological, magnetic, and electrochemical strength of the materials is also a crucial step for the protection of the material's surface. Thus, after the microstructure and phase characterization, the tribological, magnetic, and electrochemical properties of the materials are discussed in successive sections.

5. MECHANICAL PROPERTY CHARACTERIZATIONS

5.1. Experimental Calculations. The bulk hardness of the materials can be measured using a Vickers macroindenter with several numbers of indents and a fixed load and dwell time at room temperature. The diagonals of indents can be measured with optical microscopy and hardness (Hv) can be calculated using the following equation.

$$Hv = 1.854\left(\frac{P}{d^2}\right) \quad (1)$$

where P and d are the load applied and the average diagonal length, respectively. Nanomechanical dynamic modulus mapping of the samples can be performed with the normal set point force. An oscillating dynamic force ($F_{(t)} = F_O \sin \omega t$) is superimposed to the forces at a controlled lock-in frequency, where F_O is the amplitude and ω is the angular frequency ($2\pi f$) of applied set point force. A standard material of fused silica (69.6 GPa modulus and 9.25 GPa hardness) is used for the calibration of the instrument. The indenter (Berkovich diamond) has a tip radius of ∼150 nm, 0.07 Poisson ratio (ν_i), and 1141 GPa elastic modulus (E_i).[49] The images of 256 × 256 pixel resolution are obtained by the raster scan of the material's surface area through the probe. The equation of motion of the indenter for the sinusoidal indentation is $F_O \sin \omega t = mh + Ch + kh$, where k is the system's stiffness, C is its damping coefficient, and m is its mass. The measurement of a material's viscoelastic property can be achieved through modulus mapping in terms of both storage and loss modulus. The storage modulus (E') value indicates the energy that has been stored in the material and represents its elastic recovery, while the loss modulus represents the energy that has been debauched as heat and characterizes the viscous part of the material.

Nonetheless, nano hardness and reduced modulus can be assessed by a nanoindenter equipped with a diamond tip (Berkovich indenter with ∼150 nm of radius of curvature). The working principle (Figure 4a) and a typical load−displacement plot during the implementation of the indentation is shown in

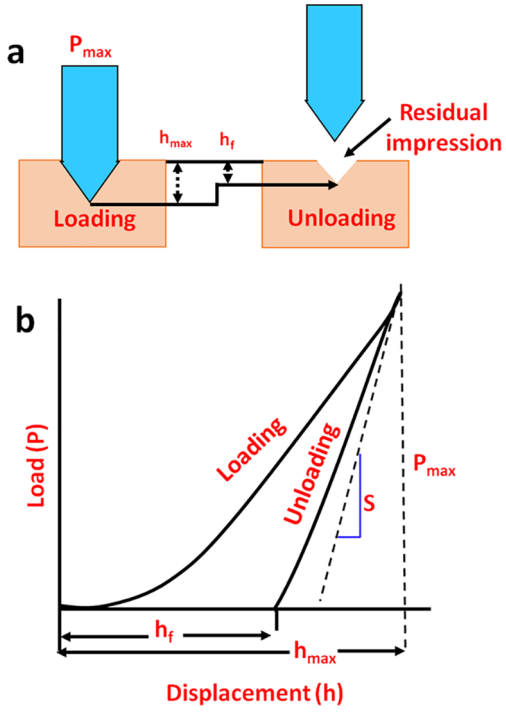

Figure 4. Schematic of (a) working principle of nanoindentation and (b) load−displacement curve showing loading and unloading. The concept was adapted from ref 50 and redrawn by the authors.

https://doi.org/10.1021/acsomega.3c09981
ACS Omega 2024, 9, 19756−19769

Figure 4b. During loading, the penetration depth rises and at extreme load, the highest penetration depth is attained. However, during unloading, as the load is decreased, the penetration depth diminishes because of elastic recovery. After the removal of the indenter, a residual impression remains that shows the plastic deformation of the material (Figure 4a). The Oliver–Pharr method (Figure 4b) is used to calculate the hardness (H) from the penetration depth

$$H = \frac{P_{max}}{A_{contact}} \tag{2}$$

The elastic modulus can be calculated using the formula

$$E_r = \left[\frac{1 - \nu_i^2}{E_i} - \frac{1 - \nu_s^2}{E_s}\right]^{-1} \tag{3}$$

where P_{max} and $A_{contact}$ are the peak indentation load and projected contact area between the indenter and the material. However, ν_i and E_i are the Poisson ratio and elastic modulus of the intender while ν_s and E_s denote the Poission ratio and elastic modulus of the sample, respectively.[49]

The experimental elastic modulus of the samples can be further compared with theoretically calculated values of the elastic modulus using various mathematical models. A depiction of theoretical calculations of the elastic modulus is given below.

5.2. Theoretical Calculations of Elastic Modulus Using Different Models. The elastic modulus was evaluated using a variety of mechanistic models, including the rule of mixing (ROM), the combined Voigt–Reuss model (V-R model), and the upper and lower bounds of the Hashin and Shtrikman (H-S) model in order to observe the impact of reinforcement implementation in composite materials.[51]

5.2.1. Rule of Mixture (ROM). The ROM offers widely disparate upper and lower bounds, and only the volume fraction of reinforcement and matrix (V_r and V_m) are taken into consideration. The transverse (upper bound) and longitudinal (lower bound) values of elastic modulus are calculated using the equations

$$E_{transverse} = V_r E_r + V_m E_m \tag{4}$$

$$E_{longitudinal} = \frac{E_m E_r}{E_m V_r + E_r V_m} \tag{5}$$

E_m, V_m and E_r, V_r are the modulus and volume fraction of matrix Ni and reinforcement, respectively.

5.2.2. Hashin and Shtrikman Model (H-S Model Upper and Lower Bounds). The H-S model predicts the elastic modulus using upper and lower bounds and includes the volume proportion of reinforcement, shear modulus of reinforcement, and matrix (G_r and G_m).

$$E_U = E_r + (1 - V_r)\left[\frac{1}{E_m - E_r} + \frac{3V_r}{3E_r + 4G_r}\right]^{-1} \tag{6}$$

$$E_L = E_m + (V_r)\left[\frac{1}{E_r - E_m} + \frac{3(1 - V_r)}{3E_m + 4G_m}\right]^{-1} \tag{7}$$

E_r, G_r and E_m, and G_m are the bulk modulus and shear modulus of reinforcement and matrix, respectively. The volume proportion of reinforcement is represented as V_r. The volume fraction of matrix is defined as $V_m = 1 - V_r$.

5.2.3. Combined Voigt–Reuss Model (V-R). The combination of transverse and longitudinal elastic moduli, obtained from ROM, provides the value of elastic modulus

$$E = \frac{3}{8}E(t) + \frac{5}{8}E(l) \tag{8}$$

$E(t)$ is the transverse modulus, and $E(l)$ is the longitudinal modulus.

6. TRIBOLOGICAL CHARACTERIZATION

6.1. Fretting Wear Estimation Using Flat-on-Disc. Fretting wear of the materials can be carried out by reciprocating friction and wear testing (Figure 5a), which employs a counter body (steel ball), a fixed load, stroke amplitude, and frequency. After the fretting test, the wear debris from the damaged surfaces of samples can be cleaned with ethanol, and a SEM scan is performed to determine the extent of damage and wear scars caused by the fretting wear of the samples. Furthermore, energy dispersive spectroscopy and an optical surface profilometer can be used to determine the degree of oxidation and surface roughness (Ra) of the samples, respectively. The working mechanism of the optical profilometer is given in Figure 5b. The wear volume, number of cycles, stroke length, and load are utilized for the calculation of wear rate (W_r).

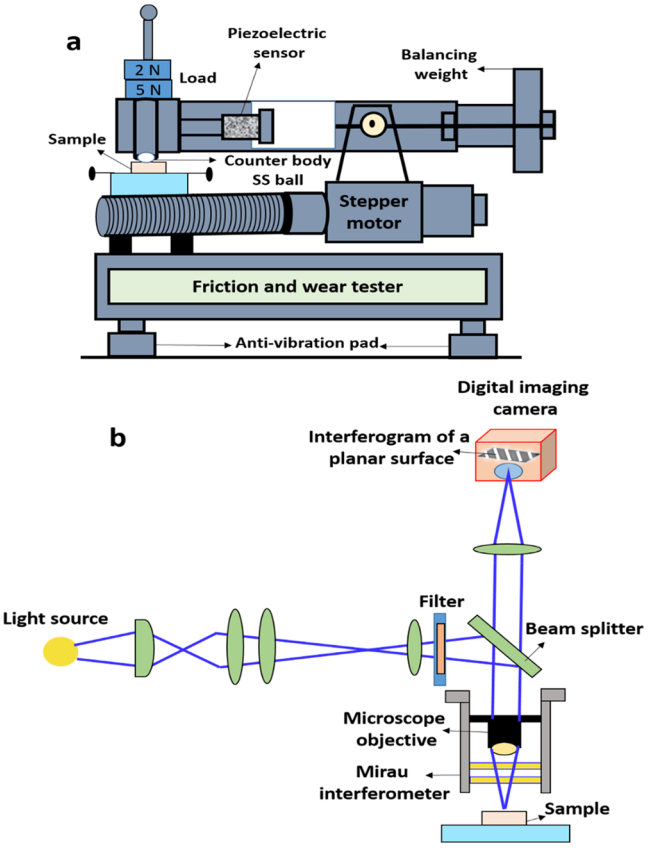

Figure 5. Schematic of (a) fretting wear setup and (b) working principle of optical profilometery. The concept was adapted from refs 52 and 53 and redrawn by the authors.

$$\text{wear rate } (W_r) = \frac{\text{wear volume}}{\text{number of cycles} \times \text{stroke length} \times \text{load}} \tag{9}$$

https://doi.org/10.1021/acsomega.3c09981
ACS Omega 2024, 9, 19756−19769

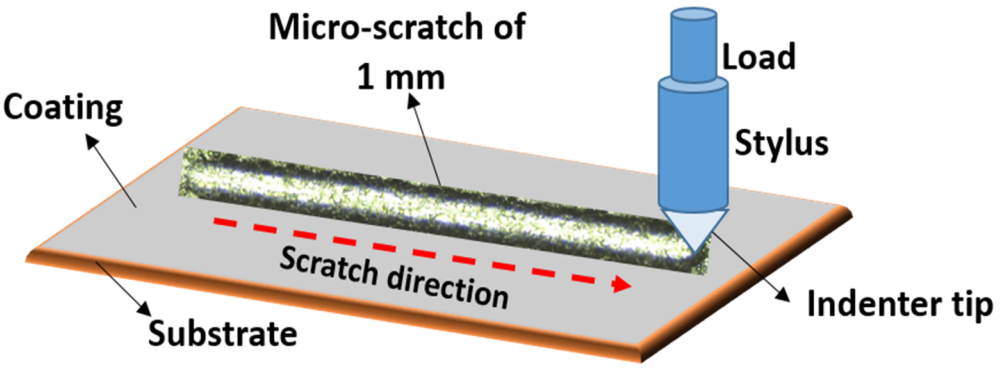

Figure 6. Schematic showing microscratch testing of coating. The concept was adapted from ref 56 and redrawn by the authors.

The wear constant (K) can be estimated using Archard's equation having wear rate (W_r), load (P), and hardness (H)

$$K = \frac{H \times W_r}{P} \tag{10}$$

6.2. Wear of Materials by Using Pin-on-Disc. The Pin-on-Disc (PoD) assessment process is a popular method for researching material sliding qualities and wear processes in various tribological settings. The Pin-on Disk tribometer is tribological characterization equipment for coatings, lubricants, and bulk materials that is accurate and reproducible. Pin-on-disk tribometers are utilized in laboratories all over the world for material benchmarking and material development. This test technique is a laboratory approach that uses a pin-on-disc arrangement to determine the wear of materials while sliding. Materials are often evaluated in dyads under nonabrasive settings. A tribometer is a device used to determine the tribological properties of two surfaces in contact, such as the coefficient of friction, friction force, and wear volume. In this arrangement, the disc spins along a vertical axis, while the pin remains motionless along the same axis. Throughout the wear test, loads can be applied manually or automatically. The pin-on-disc analyzer is one of the most common and extensively used tribotesters. It is constructed of a fixed pin that lies atop a rotating disk under the influence of dead weight. This type of tester may also be put in a climate chamber, which provides a controlled atmosphere for testing the friction and wear of various plastics and ceramic materials.[54] The pin can be any shape to replicate a certain contact; however, spherical tips are usually used to decrease the contact geometry. The coefficient of friction is considered by dividing the frictional force by the loading force of the pin. Research into the effects of sliding wear and friction qualities is quite beneficial, especially for hard coatings that are meant to enhance the lifespan of a variety of systems. Furthermore, this approach has been used in the investigation of materials used in braking systems, providing crucial insights into the unique wear processes associated with such applications. It is a commonly used technique for analyzing tribological characteristics, providing vital information on friction coefficients and wear processes, especially in diamond film applications.[54]

6.3. Scratch Testing. The scratch tester comprises a stylus and specimen stage with a spherical Rockwell indenter of 100 μm tip radius (Figure 6). By creating a scratch length on the samples' top surface, a continuous normal load is applied. The following equation can also be used to determine the volume loss or wear volume:

$$V = L[R^2 \arccos\left(1 - \frac{h}{R}\right) - (R - h)\sqrt{2Rh - h^2}] \tag{11}$$

The material's resistance against the applied load is termed as scratch hardness (H_s) and can be calculated by using an equation comprising a normal applied load (F) and a scratch width (d):[55]

$$H_s = \frac{8F}{\pi d^2} \tag{12}$$

Numerous applications at various scales, from macro- to microscale technologies, such as the tribology of multilayered materials and structures, laser texturing, micromachining, etc., can benefit greatly from multilength scale tribological investigations.[57] Increased vibrations in fretting wear can lead to catastrophic collapse of the materials (macroscale wear). Therefore, fretting wear assessment is essential to preserving the material's service life for several engineering applications.[58] On the other hand, the primary method of material failure that limits the lifetime and applicability of materials is adhesion failure, which may be evaluated quantitatively by microscratch testing (microscale tribology).[59] In order to identify the mechanism of corrosion occurring in the composite coatings, electrochemical easements are also very fundamental in terms of polarization resistance, corrosion current density, Tafel slopes, and corrosion rate. Various steps involved in the mechanism of corrosion testing are illustrated further.

7. ELECTROCHEMICAL MEASUREMENTS

The corrosion behavior of the materials can be evaluated using a 3.5 wt % NaCl solution or freely aerated borate buffer solution having a mixture of $Na_2B_4O_7{\cdot}10H_2O$, KNO_3, and H_3BO_3 using a potentiostat. The samples, saturated calomel electrode, and platinum are used as the working electrode, reference electrode, and counter electrode, respectively. The corrosion testing can be accomplished using the following different types of testing listed in the consecutive subsections.

7.1. Open Circuit Potential (OCP). The potential of the working electrode in relation to the reference electrode at which an equilibrium of anodic and cathodic reaction rates takes place in the absence of an applied voltage is known as the open circuit potential or the OCP. It is the initial step of the electrochemical measurements.

7.2. Linear Polarization and Potentiodynamic Polarization. Nondestructive linear polarization experiments are carried out in a regulated potential range and scan rate from the OCP after the OCP has stabilized. The linear polarization resistance is provided by the plot's slope. Nonetheless, corrosion current (i_{corr}) is the term used to describe the anodic or cathodic

https://doi.org/10.1021/acsomega.3c09981
ACS Omega 2024, 9, 19756−19769

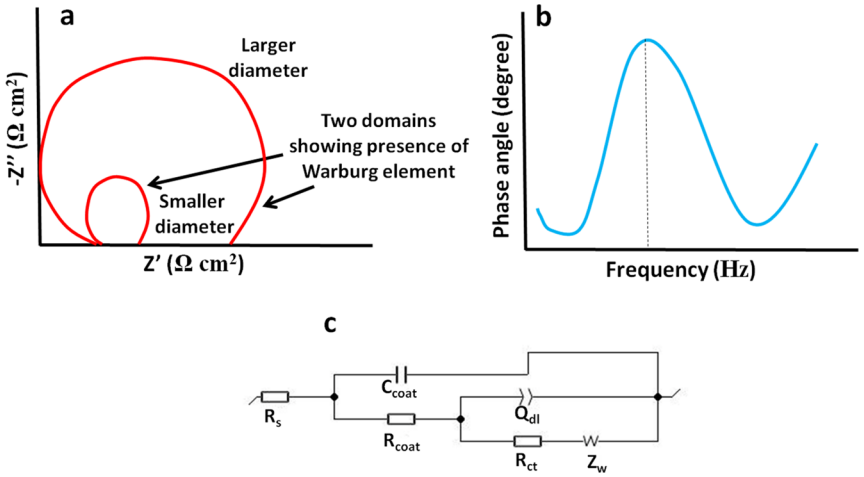

Figure 7. Schematic presentation of (a) Nyquist plot, (b) Bode phase angle plot, and (c) equivalent circuit showing various circuit elements. Original illustrations.

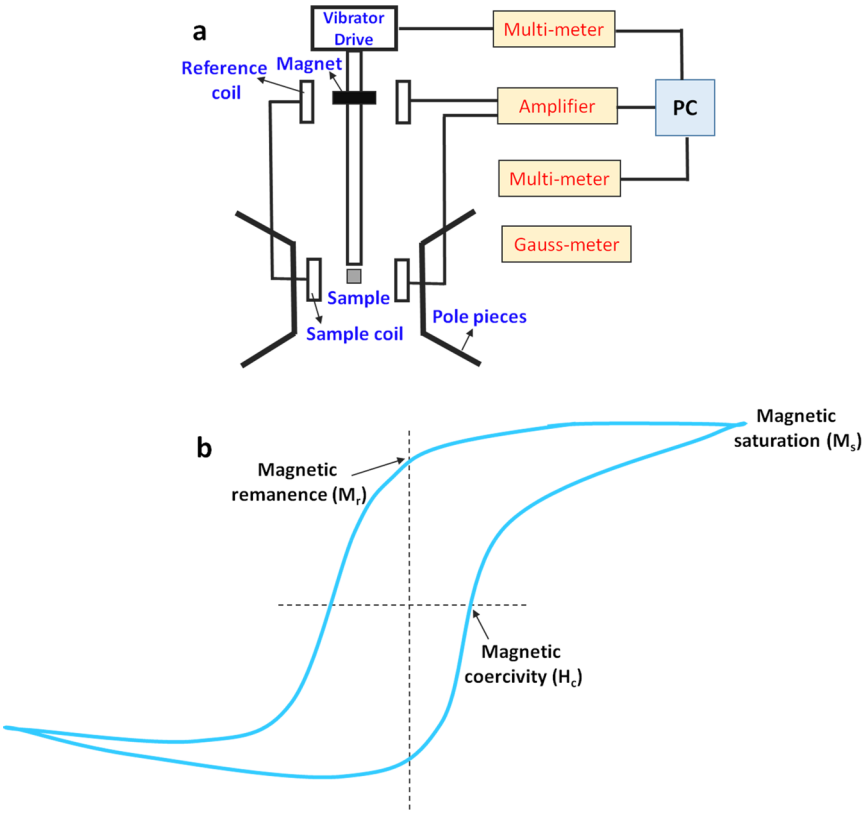

Figure 8. Schematic representation of (a) experimental setup of a VSM and (b) magnetic hysteresis loop. The concept was adapted from ref 64 and redrawn by the authors.

current value at the OCP. Potentiodynamic polarization (PD) can be scanned from the OCP at a set scan rate and potential range. By using Tafel extrapolation, the anodic and cathodic slopes (β_a and β_c, respectively) are described by the distinctive Tafel plot. Using the Stern−Geary equation, the polarization resistance from PD (R_{PD}) is calculated[60]

$$R_{PD} = \frac{\beta_a \beta_c}{2.303 i_{corr}(\beta_a + \beta_c)} \quad (13)$$

where i_{corr} is the corrosion current density and β_a and β_c are the anodic and cathodic Tafel slopes, respectively. Faraday's equation is used to calculate the material's corrosion rate (C_R)

$$C_R = K\left(\frac{i_{corr}}{\rho}\right)E_W \quad (14)$$

where $K = 3.27 \times 10^{-3}$ mm g/(μA cm year) while ρ and E_W are the density and an equivalent weight of the materials, respectively. Additionally, w_1 and w_2, which represent the corrosion rates in the absence and presence of reinforcements, respectively, can be used to determine the change in the

https://doi.org/10.1021/acsomega.3c09981
ACS Omega 2024, 9, 19756−19769

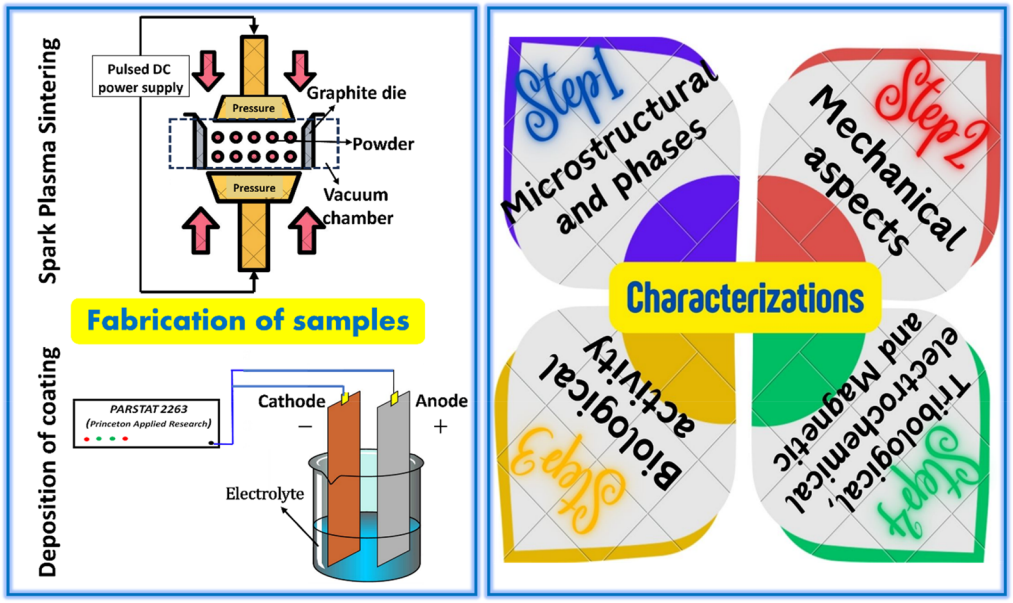

Figure 9. Bird's eye view of the review.

percentage corrosion inhibition efficiency ($\%_{CIE}$) with reinforcements.[61]

$$\%_{CIE} = \left[1 - \frac{w_2}{w_1}\right] \times 100 \tag{15}$$

Besides linear polarization (LP) and potentiodynamic polarization (PD), electrochemical impedance spectroscopy is used to further estimate the corrosion resistance with the assessment of the elements of the Nyquist plot, Bode plot, and equivalent circuits.

7.3. Electrochemical Impedance Spectroscopy (EIS). An alternating signal of small amplitude is applied to an electrode dipped into an electrolyte for comparing the initial disturbance (described as disturbance potential ΔE) and response (current ΔI) of the electrode by measuring the phase shift and amplitude of current and voltage. Electrochemical impedance spectroscopy (EIS) can be carried out in various ranges of frequency sweep and sinusoidal potential perturbation at OCP.

The impedance (Z) measures the relationship between ΔE and ΔI. EIS provides the distinctive Nyquist plot (Figure 7a), Bode plot with impedance modulus, and phase angle plot (Figure 7b). The Nyquist plot measures the real (Z') and imaginary (Z'') portions of impedance at different frequencies entails the sequence of points and signifies the extent and direction of the impedance vector with a particular frequency. The larger diameter of the Nyquist plot signifies the charge transfer resistance (R_{ct}), equivalent to the polarization resistance (R_{EIS}) and thus a lower corrosion rate. The Bode plot displays the logarithm of impedance modulus and phase shift as the function of the logarithm of the frequency sweep. The equivalent circuit (Figure 7c) depends on the corrosion process and, thus, contains various circuit elements. The solution resistance R_s, coating resistance R_{coat}, coating capacitance C_{coat}, and charge transfer resistance R_{ct} for the region where corrosion occurs are the main components associated with the Nyquist plot. For an improved fit, the corresponding circuit is changed to include the Warburg impedance Z_w and the constant phase element Q_{dl}. The charge separation between the metal and electrolyte interface is characterized by the frequency-dependent parameter Q_{dl}[62] and the presence of Warburg impedance is indicated by two separate domains on the Nyquist plot, which are ascribed to the metal substrate, and diffusion information.[63]

Later than an assortment of electrochemical characterizations, the assessment of the magnetic properties for different types of materials is reviewed further.

8. MAGNETIC PROPERTY CHARACTERIZATION

The samples' saturation magnetization (M_s), magnetic coercivity (H_c), and remanence (M_r) are assessed using a vibrating sample magnetometer (VSM). The basis of VSM's operation is Faraday's law of magnetic induction in which an electromagnetic force is produced in a coil when the change in flux occurs through the coil. In the measurement setup, the sample is moved in the proximity of two pickup coils (Figure 8a), which results in the formation of a magnetic hysteresis loop with the ferromagnetic sample (Figure 8b). The presence of magnetic domains in the materials is ascribed to the magnetic hysteresis loop. The technique of magnetic force microscopy, which is based on atomic force microscopy, is employed to identify the magnetization hysteresis curves of the samples' ferromagnetic particles. There is surface magnetization in these domains. The domain walls are shown as dark areas, and the primary domains are shown as light areas. The width of the domain wall is given by the average of the MFM amplitude maxima. It is also possible to compute the magnetostatic energy per unit area (e_{ms}) using the magnetic saturation (M_s) and domain wall width (W).

$$e_{ms} = 0.85W(M_s)^2 \tag{16}$$

9. BIOLOGICAL CHARACTERIZATION

The process of developing, preserving, and efficiently managing certain biological features within a specified system is known as biological characterization. When referring to the scaffold matrix, it should provide an environment conducive to cellular activity, such as cell adhesion, migration, and function, as well as facilitate vascularization while giving adequate room for tissue

https://doi.org/10.1021/acsomega.3c09981
ACS Omega 2024, 9, 19756−19769

development. The cell carrier's principal goal is to promote processes that resemble the physiology of the organism. The control of the dynamic balance between bone tissue degradation and bone tissue growth is a critical part of scaffold engineering. Prolonged resorption can stymie bone renewal, whereas early breakdown can encourage the development of physiologically more potent tissues such as connective tissue. As a result, a perfect material should be compatible with the biological functions of the tissue in which it is administered.[65]

Figure 9 presents the debriefing of the review in terms of the fabrication of samples and their characterizations. The samples can be frequently prepared by spark plasma sintering and deposition techniques in the form of pellets and coatings. The synthesis of samples leads to a characterization process, which can be done in four different steps. *Step I*: review the discussion of the different mechanics with respect to each reinforcement and a correlative investigation of microstructural and phase characterizations of prepared samples in the form of coatings or pellets with various reinforcements on the same processing parameter. *Step II*: the highlights of the experimental and theoretical aspects of the mechanical properties of the materials. *Step III*: the deliberations on the tribological, electrochemical, and magnetic characteristics of the samples. *Step IV*: biological activity of the materials.

10. CONCLUSIONS AND OUTLOOK

In summary, the review sheds light on the different fabrication and characterization methods of the materials, which are the elementary basis of any research. Prior to the discussion of characterization processes, the initial highlights of the review involved fabrication techniques of composite samples (coatings or pellets) by using spark plasma sintering and deposition methods. The discussion on the determination of the top surface morphology and phase retention of the materials by microstructural analysis and phase characterizations was embraced in the review. The nanoindentation technique for experimental mechanical characterizations of the materials was described with a working principle and mechanism. The experimental results can be compared with the various theoretical models for elastic modulus calculations of the samples, and their illustration altogether can be valuable for the readers. Further, in order to compare the wear and corrosion resistance of the materials, the report demonstrated the tribological and electrochemical testing using microscratch and LP, PD, and EIS studies, respectively. However, a brief deliberation on the magnetic studies was carried out for the evolution of magnetic saturation, coercivity, and remanence of the materials using a vibrating sample magnetometer along with the visualization of the magnetic domains present in the materials using magnetic force microscopy. Additionally, the multiscale wear mechanism was established using flat-on-disc, pin-on-disc, and microscratch testing. Voronoi tessellation was exemplified for the comprehensive study of distance and area between nanoparticles when varying concentrations of nanoparticles were applied in the bulk matrix. Thus, in order to be of great significance to chemists, materials scientists, physicists, and innovators working in the field of materials, as well as to raise awareness among a global audience (beginners as well as nonspecialists), this review aims to be thorough, authoritative, critical, and accessible to the materials community in general.

AUTHOR INFORMATION

Corresponding Authors

Shikha Awasthi − *Department of Chemistry, School of Basic Sciences, Manipal University Jaipur, Jaipur 303007 Rajasthan, India*; orcid.org/0000-0003-1604-8087; Email: shikha.awasthi@jaipur.manipal.edu

Suranjan De − *Department of Chemistry, School of Basic Sciences, Manipal University Jaipur, Jaipur 303007 Rajasthan, India*; Email: suranjan.de@jaipur.manipal.edu

Sarvesh Kumar Pandey − *Department of Chemistry, Maulana Azad National Institute of Technology, Bhopal 462003 Madhya Pradesh, India*; Email: skpchmiitk@gmail.com

Complete contact information is available at: https://pubs.acs.org/10.1021/acsomega.3c09981

Notes

The authors declare no competing financial interest.

ACKNOWLEDGMENTS

The authors thank the Department of Chemistry, Manipal University Jaipur.

REFERENCES

(1) Farhoodi, M. Nanocomposite Materials for Food Packaging Applications: Characterization and Safety Evaluation. *Food Engineering Reviews* **2016**, *8*, 35−51.

(2) Nguyen-Tri, P.; Nguyen, T. A.; Carriere, P.; Ngo Xuan, C. Nanocomposite Coatings: Preparation, Characterization, Properties, and Applications. *International Journal of Corrosion* **2018**, *2018*, 1−19.

(3) Sanchez, C.; Soler-Illia, G.J. de A.A.; Ribot, F.; Lalot, T.; Mayer, C. R.; Cabuil, V. Designed Hybrid Organic−Inorganic Nanocomposites from Functional Nanobuilding Blocks. *Chem. Mater.* **2001**, *13*, 3061−3083.

(4) Sanchez, C.; Julián, B.; Belleville, P.; Popall, M. Applications of hybrid organic−inorganic nanocomposites. *J. Mater. Chem.* **2005**, *15*, 3559.

(5) Omanović-Mikličanin, E.; Badnjević, A.; Kazlagić, A.; Hajlovac, M. Nanocomposites: a brief review. *Health Technol. (Berl)* **2020**, *10*, 51−59.

(6) Schmidt, D.; Shah, D.; Giannelis, E. P. New advances in polymer/layered silicate nanocomposites. *Curr. Opin Solid State Mater. Sci.* **2002**, *6*, 205−212.

(7) Wang, R. M.; Zheng, S. R.; Zheng, Y. P. *Polymer matrix composites and technology*; Woodhead Publishing Limited and Science Press Limited: 2011.

(8) Yao, Q.; Chen, L.; Zhang, W.; Liufu, S.; Chen, X. Enhanced Thermoelectric Performance of Single-Walled Carbon Nanotubes/Polyaniline Hybrid Nanocomposites. *ACS Nano* **2010**, *4*, 2445−2451.

(9) Zhang, H.; Zhong, X.; Xu, J.-J.; Chen, H.-Y. Fe3O4/polypyrrole/Au nanocomposites with core/shell/shell structure: synthesis, characterization, and their electrochemical properties. *Langmuir* **2008**, *24*, 13748−13752.

(10) Ruecha, N.; Rangkupan, R.; Rodthongkum, N.; Chailapakul, O. Novel paper-based cholesterol biosensor using graphene/polyvinylpyrrolidone/polyaniline nanocomposite. *Biosens Bioelectron* **2014**, *52*, 13−19.

(11) Zhang, W.-D.; Xu, B.; Jiang, L.-C. Functional hybrid materials based on carbon nanotubes and metal oxides. *J. Mater. Chem.* **2010**, *20*, 6383.

(12) Wang, G.-X.; Zhang, B.-L.; Yu, Z.-L.; Qu, M.-Z. Manganese oxide/MWNTs composite electrodes for supercapacitors. *Solid State Ion* **2005**, *176*, 1169−1174.

(13) Liu, B.; Chen, J. H.; Xiao, C. H.; Cui, K. Z.; Yang, L.; Pang, H. L.; Kuang, Y. F. Preparation of Pt/MgO/CNT Hybrid Catalysts and Their Electrocatalytic Properties for Ethanol Electrooxidation. *Energy Fuels* **2007**, *21*, 1365−1369.

https://doi.org/10.1021/acsomega.3c09981
ACS Omega 2024, 9, 19756−19769

(14) Kongkanand, A.; Kamat, P. V. Electron Storage in Single Wall Carbon Nanotubes. Fermi Level Equilibration in Semiconductor−SWCNT Suspensions. *ACS Nano* **2007**, *1*, 13−21.
(15) Harmer, M. P.; Chan, H. M.; Miller, G. A. Unique Opportunities for Microstructural Engineering with Duplex and Laminar Ceramic Composites. *J. Am. Ceram. Soc.* **1992**, *75*, 1715−1728.
(16) Becher, P. F. Microstructural Design of Toughened Ceramics. *J. Am. Ceram. Soc.* **1991**, *74*, 255−269.
(17) LANGE, F. F. Effect of Microstructure on Strength of Si_3N_4-SiC Composite System. *J. Am. Ceram. Soc.* **1973**, *56*, 445−450.
(18) Burnett, T. L.; Withers, P. J. Completing the picture through correlative characterization. *Nat. Mater.* **2019**, *18*, 1041−1049.
(19) Mourdikoudis, S.; Pallares, R. M.; Thanh, N. T. K. Characterization techniques for nanoparticles: comparison and complementarity upon studying nanoparticle properties. *Nanoscale* **2018**, *10*, 12871−12934.
(20) Raj, B. A perspective on materials characterization for technology advancement and industrial growth: Emphasis on non-destructive evaluation. *Bulletin of Materials Science* **1996**, *19*, 839−855.
(21) Cavaliere, P.; Sadeghi, B.; Shabani, A. Spark Plasma Sintering: Process Fundamentals, in: *Spark Plasma Sintering of Materials*; Springer International Publishing: 2019: pp 3−20. DOI: 10.1007/978-3-030-05327-7_1.
(22) Seok, J.W.; Jadeed, N.M.; Lin, R.Y. Sputter-deposited nanocrystalline Cr and CrN coatings on steels. *Surf. Coat. Technol.* **2001**, *138*, 14−22.
(23) Zubielewicz, M.; Królikowska, A. The influence of ageing of epoxy coatings on adhesion of polyurethane topcoats and protective properties of coating systems. *Prog. Org. Coat.* **2009**, *66*, 129−136.
(24) Awasthi, S.; Pandey, S.K.; Pandey, C.P.; Balani, K. Progress in Electrochemical and Electrophoretic Deposition of Nickel with Carbonaceous Allotropes: A Review. *Adv. Mater. Interfaces* **2020**, *7*, 1901096.
(25) Low, C. T. J.; Walsh, F.C. Self-lubricating Metal Composite Coatings by Electrodeposition or Electroless Deposition. *Encyclopedia of Tribology*; Springer: 2013.
(26) Kerr, C.; Barker, D.; Walsh, F.; Archer, J. The Electrodeposition of Composite Coatings based on Metal Matrix-Included Particle Deposits. *Transactions of the IMF* **2000**, *78*, 171−178.
(27) Wasekar, N. P.; Latha, S. M.; Ramakrishna, M.; Rao, D. S.; Sundararajan, G. Pulsed electrodeposition and mechanical properties of Ni-W/SiC nano-composite coatings. *Mater. Des* **2016**, *112*, 140−150.
(28) Wang, S.; Zhou, N.; Walsh, F. C. Diverse electrodeposits from modified acid sulphate (Watts nickel) baths. *Transactions of the Institute of Metal Finishing* **2016**, *94*, 274−282.
(29) Nielsch, K.; Muller, F.; Li, A.-P.; Gosele, U. Uniform Nickel Deposition into Ordered Alumina Pores by Pulsed Electrodeposiiton. *Adv. Mater.* **2000**, *12*, 582−586.
(30) Bhardwaj, M.; Balani, K.; Balasubramaniam, R.; Pandey, S.; Agarwal, A. Effect of current density and grain refining agents on pulsed electrodeposition of nanocrystalline nickel. *Surface Engineering* **2011**, *27*, 642−648.
(31) Wasekar, N. P.; Latha, S. M.; Ramakrishna, M.; Rao, D. S.; Sundararajan, G. Pulsed electrodeposition and mechanical properties of Ni-W/SiC nano-composite coatings. *Mater. Des* **2016**, *112*, 140−150.
(32) LU, J.; YANG, Q.-h.; ZHANG, Z. Effects of additives on nickel electrowinning from sulfate system, Trans. *Nonferrous Met. Soc. China.* **2010**, *20*, s97−s101.
(33) Fahami, A.; Nasiri-tabrizi, B.; Rostami, M.; Ebrahimi-kahrizsangi, R. Influence of surfactants on the characteristics of nickel matrix nNanocomposite coatings. *ISRN Electrochemistry* **2013**, *2013*, 1−8.
(34) Wang, D.; Li, F.; Shi, Y.; Liu, M.; Liu, B.; Chang, Q. Optimization of the Preparation Parameters of High-Strength Nickel Layers by Electrodeposition on Mild Steel Substrates. *Materials* **2021**, *14*, 5461.
(35) Hickling, A. Studies in electrode polarisation. Part IV.—The automatic control of the potential of a working electrode. *Trans. Faraday Soc.* **1942**, *38*, 27−33.
(36) Fotovvati, B.; Namdari, N.; Dehghanghadikolaei, A. On Coating Techniques for Surface Protection: A Review. *Journal of Manufacturing and Materials Processing* **2019**, *3*, 28.
(37) Kramer, M.S.; Byrnes, L.E.; Holmes, G.L., Method and Apparatus for Application of Thermal Spray Coatings to Engine Blocks, U.S. Patent 5271967, 1993.
(38) Ebnesajjad, S., Surface and Material Characterization Techniques. In: *Handbook of Adhesives and Surface Preparation*; Elsevier: 2011; pp 31−48. DOI: 10.1016/B978-1-4377-4461-3.10004-5.
(39) Gonzalez, R. E. PARAVT: Parallel Voronoi Tessellation code. *Astronomy and Computing* **2016**, *17*, 80.
(40) Awasthi, S.; Pandey, S. K.; Gaur, J. K.; Srivastava, C. Load-bearing study and interfacial interactions of hydroxyapatite composite coatings for bone tissue engineering. *Mater. Chem. Front* **2022**, *6*, 3731−3747.
(41) Awasthi, S.; Gaur, J. K.; Bobji, M. S. Advanced Ferrogels with High Magnetic Response and Wear Resistance Using Carbon Nanotubes. *J. Alloys Compd.* **2020**, *848*, 156259−156269.
(42) Kowalczuk, D.; Pitucha, M. Application of FTIR Method for the Assessment of Immobilization of Active Substances in the Matrix of Biomedical Materials. *Materials* **2019**, *12*, 2972.
(43) Ferrari, A. C. Raman spectroscopy of graphene and graphite: Disorder, electron−phonon coupling, doping and nonadiabatic effects. *Solid State Commun.* **2007**, *143*, 47−57.
(44) Saito, R.; Takeya, T.; Kimura, T.; Dresselhaus, G.; Dresselhaus, M. S. Raman intensity of single-wall carbon nanotubes. *Phys. Rev. B* **1998**, *57*, 4145−4153.
(45) Ferrari, A. C.; Robertson, J. Resonant Raman spectroscopy of disordered, amorphous, and diamondlike carbon. *Phys. Rev. B* **2001**, *64*, 075414.
(46) Agrawal, G.; Samal, S. K. Raman Spectroscopy for Advanced Polymeric Biomaterials. *ACS Biomater Sci. Eng.* **2018**, *4*, 1285−1299.
(47) Tan, P.; Deng, Y.; Zhao, Q. Temperature-dependent Raman spectra and anomalous Raman phenomenon of highly oriented pyrolytic graphite. *Phys. Rev. B* **1998**, *58*, 5435−5439.
(48) Tan, P.; Hu, C.; Dong, J.; Shen, W.; Zhang, B. Polarization properties, high-order Raman spectra, and frequency asymmetry between Stokes and anti-Stokes scattering of Raman modes in a graphite whisker. *Phys. Rev. B* **2001**, *64*, 214301.
(49) Oliver, W. C.; Pharr, G. M. Measurement of Hardness and Elastic Modulus by Instrumented Indentation: Advances in Understanding and Refinements to Methodology. *J. Mater. Res.* **2004**, *19*, 3−20.
(50) He, R.; Gahlawat, S.; Guo, C.; Chen, S.; Dahal, T.; Zhang, H.; Liu, W.; Zhang, Q.; Chere, E.; White, K.; Ren, Z. Studies on mechanical properties of thermoelectric materials by nanoindentation. *Physica Status Solidi (a)* **2015**, *212*, 2191−2195.
(51) Hu, H.; Onyebueke, L.; Abatan, A. Characterizing and modeling mechanical properties of nanocomposites- review and evaluation. *Journal of Minerals & Materials Characterization & Engineering* **2010**, *09*, 275−319.
(52) Kim, H.-K.; Kim, S.-J.; Yoon, K.-H.; Kang, H.-S.; Song, K.-N. Fretting wear of laterally supported tube. *Wear* **2001**, *250*, 535−543.
(53) Baysan, A.; Sleibi, A.; Ozel, B.; Anderson, P. The quantification of surface roughness on root caries using Noncontact Optical Profilometry—An in vitro study. *Lasers Dent Sci.* **2018**, *2*, 229−237.
(54) Federici, M.; Straffelini, G.; Gialanella, S. Pin-on-Disc Testing of Low-Metallic Friction Material Sliding Against HVOF Coated Cast Iron: Modelling of the Contact Temperature Evolution. *Tribol Lett.* **2017**, *65*, 121.
(55) Narasimman, P.; Pushpavanam, M.; Periasamy, V. M. Wear and scratch resistance characteristics of electrodeposited nickel-nano and micro SiC composites. *Wear* **2012**, *292−293*, 197−206.
(56) Kim, K.-S.; Kim, Y.; Jung, S.-B. Microstructure and adhesion characteristics of a silver nanopaste screen-printed on Si substrate. *Nanoscale Res. Lett.* **2012**, *7*, 49.
(57) El Mansori, M. Special issue collection on tribology in multi-scale manufacturing. *Surf. Topogr* **2017**, *5*, 010301.
(58) Sikdar, K.; Shekhar, S.; Balani, K. Fretting wear of Mg-Li-Al based alloys. *Wear* **2014**, *318*, 177−187.

https://doi.org/10.1021/acsomega.3c09981
ACS Omega 2024, 9, 19756−19769

(59) Meneve, J. In *Adhesion Measurement of Films and Coatings*; Mittal, K. L., Ed.; VSP BV: 2001; Vol. 2.
(60) Franco, M.; Hari Krishna, T.; Pillai, A. M.; Rajendra, A.; Sharma, A. K. A comparative study on the corrosion behaviour of hard anodic coatings on AA 6061 obtained using DC and pulsed DC power sources. *Acta Metallurgica Sinica* **2013**, *26*, 647−656.
(61) Ebadi, M.; Basirun, W. J.; Leng, S. Y.; Mahmoudian, M. R. Investigation of corrosion inhibition properties of caffeine on nickel by electrochemical techniques. *Int. J. Electrochem Sci.* **2012**, *7*, 8052−8063.
(62) Chen, Y.; Hong, T.; Gopal, M.; Jepson, W. P. EIS studies of a corrosion inhibitor behavior under multiphase flow conditions. *Corros. Sci.* **2000**, *42*, 979−990.
(63) Walter, G. W. The application of impedance spectroscopy to study the uptake of sodium chloride solution in painted metals. *Corros. Sci.* **1991**, *32*, 1041−1058.
(64) Adeyeye, A.O.; Shimon, G. Growth and Characterization of Magnetic Thin Film and Nanostructures. *Handbook of Surface Science* **2015**, *5*, 1−41.
(65) Markovic, D.; Petrovic, B.; Jokanovic, V.; Peric, T.; Colovic, B.; Karadzic, I. Nanomaterials as scaffolds in bone tissue engineering in dental medicine. In *Nanobiomaterials in Hard Tissue Engineering*; Elsevier: 2016: pp 413−442. DOI: 10.1016/B978-0-323-42862-0.00014-6.

https://doi.org/10.1021/acsomega.3c09981
ACS Omega 2024, 9, 19756−19769